metals

MDPI

Article

Structural Peculiarities of Growth and Deformation of Ti-Al-Si-Cu-N Gradient-Laminated Coatings Due to Indentation

Stanislav Ovchinnikov [1,*] and Vladimir Kuznetsov [1,2]

[1] Institute of Strength Physics and Material Science, Siberian Division, Russian Academy of Sciences, 634055 Tomsk, Russia; kuznetsov@rec.tsu.ru
[2] Faculty of Physics, Tomsk State University, 634050 Tomsk, Russia
* Correspondence: ovmlmpin@ispms.tsc.ru

Abstract: The composition, structure, properties and deformation behavior during the indentation of gradient-layered heterophase coatings of a Ti-Al-Si-Cu-N system were studied using scanning, transmission microscopy and hardness measurement techniques. The results showed the alteration of structural state characteristics—decreased crystal sizes and crystal lattice parameter and increased lattice bending–torsion—throughout the coating thickness, which changed depending on the elemental composition and the synthesis conditions. The work also studied the coating's fracture behavior and assessed the macroscopic plastic deformation of its separate layers. It was established that near the indenter's tip, the nanocrystalline structure experienced the formation of separate nanosized localized fracture areas that were connected by multiple branching cracks. It was shown that the deformation of nanocrystalline and submicrocrystalline layers may exceed dozens of percent, and more in magnitude, especially with increasing distance from the indentation tip in the case of a layer with a columnar structure. The characteristics of the microstructure of different coating layers in the indentation zone were studied. It was found that in the indentation zone under the indenter's tip, the deformation of layers with initially different structures led to equalization of the characteristics of their structural state and the similarity of a defective microstructure at the nanoscale level.

Keywords: gradient-laminated coatings; nanoindentation; electron microscopy; nanocrystals; columnar grains; rotational deformation mode

Citation: Ovchinnikov, S.; Kuznetsov, V. Structural Peculiarities of Growth and Deformation of Ti-Al-Si-Cu-N Gradient-Laminated Coatings Due to Indentation. *Metals* **2022**, *12*, 626. https://doi.org/10.3390/met12040626

Academic Editors: Maciej Motyka and Thomas Gries

Received: 10 December 2021
Accepted: 30 March 2022
Published: 4 April 2022

1. Introduction

As of today, the synthesis of wear-resistant and protective coatings should be scientifically justified by the experimental identification of regularities in their deformation and fracture under different testing conditions by studying the peculiarities and mechanisms of their structure modification. The most conclusive, but complex, way to receive such data is the investigation of nonequilibrium multi-element nanocomposite coatings with a gradient-laminated structure. Based on this, the most reasonable method to use involves model tests (indentation, for instance) because they propose a wide range of variable parameters and mimic operational conditions (wear of coatings, in particular).

In the case of wear-resistant coatings, promising compositions are those that form a nanocomposite structure with appreciably different strengths between the composing phases (fracture toughness) and provide controlled alteration of their volumetric ratios and properties via alloying. Therefore, of particular interest are MeN/a-phase/Me coatings, where MeN is a hard nitride of a transition metal, Me is a metal that is insoluble in the nitride and a-phase is an amorphous grain-boundary phase.

In the aforementioned composites with silicon, the strength properties can be further enhanced and stabilized by the formation of a structure with a strong bond between its metal nitride and silicon nitride [1]. Furthermore, decreased dimensions of crystals after

such alloying can positively affect the segregation and precipitation of metal crystals due to a decreased diffusion distance and increased density of defect regions (crystal boundaries). Such regulation of the volumetric fraction of the metal phase in a nanocomposite may increase its fracture toughness.

Moreover, the optimal—from the perspective of combined plasticity and strength of the coating—structure is achievable after investigating the peculiarities and mechanisms of deformation. Based on this, we should note that due to the low plasticity of nitride coatings, the main mechanism of their deformation on the indentation on soft substrates (steel) is the formation of various (radial, inclined, edge) cracks and shear creep along the boundaries of columnar crystals [2–4]. Existing data on the modification of the defect microstructure in the indentation zone are scarce and, to some extent, controversial.

For instance, in [2–8], which examined indentation zones using electron microscopy, the authors stated in the dislocations density research that the action of the dislocation deformation mechanisms was not detected. However, in [7], the authors discovered the effect of material press out along the periphery of the indentation and material bending within the indentation due to the generation of geometrically necessary dislocations and the relaxation of stresses in the zones of transverse cracks via dislocation movement. Wu [9] noted the increase in dislocation density in columnar crystals under the indenter's tip. These data, along with [10,11], in relation to columnar crystals and laminar structures testify to the development of mechanically loaded coatings of rotational deformation modes, where structural mechanisms in coatings have not been experimentally identified yet. Furthermore, the indentation of laminar structures with different properties of composing layers revealed the formation of bands of localized shear [12,13].

Thus, on the one hand, the results show the possibility of initiating plastic deformations in coatings by altering the stress state scheme, modifying the level of indentation-induced stresses through variation of the substrate strength and forming a heterophase nanocrystalline structure with considerably different strength properties of composing components. On the other hand, there is a lack of experimental data connecting deformation phenomena with the peculiarities of defect microstructure modification at submicro- and nanoscales.

Therefore, the present work studied the peculiarities of deformation and fracture regarding indentation using the example of a gradient-laminated Ti-Al-Si-Cu-N coating, which combines layers of submicrocrystalline columnar grains and a nanocrystalline structure containing metal inclusions. The chosen architecture and coating composition allowed for controllable alteration of the fracture mechanisms and fracture toughness. To determine them, we used transmission electron microscopy (TEM) to characterize the structural peculiarities of deformation and fracture at different scales, including a quantitative estimation of crystal lattice orientation alteration. This allowed for identifying the specific character of the deformation state (development of rotational modes) in separate nanocrystals in the most deformed region under the indenter's tip.

2. Materials and Methods

The scheme of the unit for the coatings deposition is shown in Figure 1. Gradient laminar Ti-Al-Si-Cu-N coatings were obtained via unbalanced magnetron sputtering of targets from Ti (VT 1-0 alloy, wt%: Ti—99.24–99.7%, Fe—up to 0.25%, C—up to 0.07%, Si—up to 0.1%, N—up to 0.04%, O—up to 0.2%, H—up to 0.01%) manufactured by VSMPO-AVISMA Corporation (Berezniki, Russia), cold-pressed $Al_{60}Si_{40}$ alloy (wt.%: Al—59.10%, Si—40.7%, O—up to 0.2%) from RUSAL Novokuznetsk Aluminum Plant (Novoruznetsk, Russia) and commercial copper (M1 alloy, wt%: Cu—99.90%, Fe—0.005%, Ni—0.004%, Zn—0.005%, Sn—003%, Sb—0.002%, As—0.002%, S—0.004%, Pb—0.005%, O—0.07%) from UMMC (Verhnyaya Pyshma, Russia).

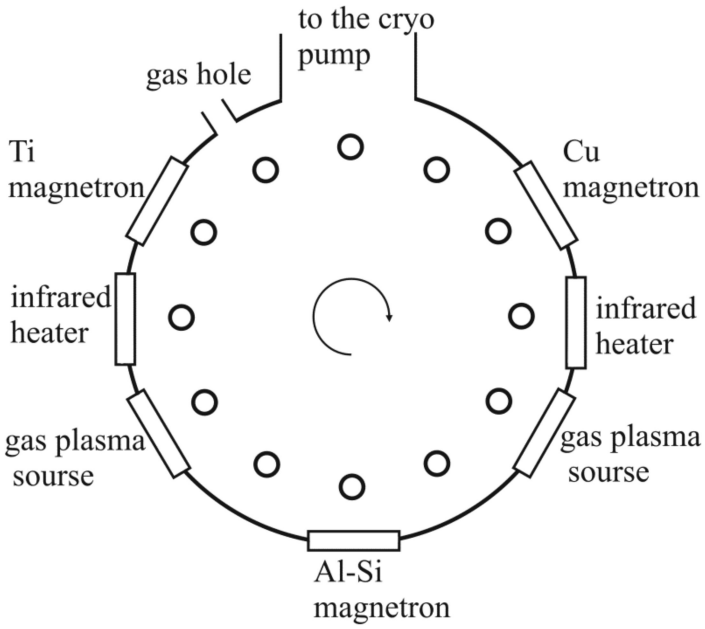

Figure 1. The scheme of the unit for the coatings deposition.

The coatings were deposited onto substrates from T15K6 hard alloy (wt%: WC—79%, TiC—15%, Co—6%) and 316L stainless steel in the mixture of argon and nitrogen with a flow ratio of 3:1, a total pressure of ≈0.1 Pa and a temperature of 150 °C. Before the coating application, the T15K6 alloy substrates were mechanically polished and 316L steel substrates were electrolytically polished and ultrasonically washed in ethanol and deionized water. After cleaning the substrates using Ar ions under a bias potential of −300 V, a Ti sublayer was deposited on them, which was then nitrated under a bias potential of 6 kV.

The coatings were synthesized in two stages. At stage one, on the nitrated titanium sublayer, a TiN layer was grown at a titanium target sputtering power of 1.8 kW. When depositing alloyed layers of titanium nitride, the titanium target sputtering power was constant (1.8 kW), while the sputtering power for Al-Si and Cu targets was altered within the range of 0.1–0.7 kW with a step size of ≈0.05 kW, with a corresponding increase in the reaction gas feeding rate. During the deposition of the layers, the sputtering of targets was assisted by a plasma generator of gas ions at a current of ≈150 mA and a bias potential on the substrates of −300 V. The resulting coatings thickness was ≈1.1 μm.

We used a Quanta 200 3D Electron Microscope (FEI, Hillsboro, OR, USA) to study the morphology of the surface within the indentation regions and obtain cross-sections of the foils using the focused ion beam (FIB) method. The TEM analysis was performed on a JEM-2100 Electron Microscope (JEOL, Tokyo, Japan). This instrument was also used to determine the elemental composition of the coatings using energy-dispersive X-ray spectroscopy (EDXS). The nanohardness of the coatings was assessed in 10 measurements via the Oliver–Pharr method [14] using a Table Top Nanoindentation Tester (TTX-NHT^2) (Anton Paar GmbH, Graz, Austria) with a Berkovich indenter with a load varying from 5 mN (indentation depth of approximately 1/10 of the coating thickness) to 400 mN.

The structural state of the coating in terms of the development of the rotational deformation mode under indentation was characterized using dark-field analysis of crystal lattice bending–torsion, which allowed for assessing the alteration of the orientation of crystal local volumes via the movement of the bending extinction contours (see details in [15,16]). The quantitative estimates of this approach are connected with the calculation of the components of the crystal lattice bending–torsion tensor χ_{ij}, whose values reflect the altered orientation of reflecting surfaces under displacement of the contour in direction $\vec{i}$

due to crystal rotation around axis $\vec{j}$ in the laboratory frame of reference. The choice of the said axes was due to the convenience of their usage.

This work exclusively estimated the values of component χ_{21}, which demonstrated the bending of the plane perpendicular to the electron beam in the directions lying in the foil's plane. It is known from [15] that

$$\chi_{21} = \Delta\varphi \times \sin\beta / r \quad (1)$$

where $\Delta\varphi$ is the alteration of the specimen inclination angle, β is the angle between the inclination axis projection and the direction of the normal to the reflecting plane and r is the displacement of the extinction contour on inclination. In addition, the work mentions and qualitatively assesses component χ_{31} of the tensor that characterizes the bending of reflecting planes in the electron beam propagation direction.

3. Results and Discussion

3.1. Coating Structure after Deposition

The alteration of the synthesis conditions during coating growth determines the formation of a gradient laminar structure with well-pronounced prolonged interfaces between the layers of non-alloyed and alloyed TiN nitride and between its different structural states: with submicrocrystalline columnar grains and with a nanocrystalline structure (Figure 2). The transverse cross-section of the structure showed non-planar interfaces between the layers (e.g., the boundary between layers 2 and 3 in Figure 2a,b), while the surface demonstrated a less profound relief. This testified to both competing columnar growth and equalization of the growth rate in the nanocrystalline coating layer, which was, probably, promoted by the effects of secondary sputtering from the surface ridges.

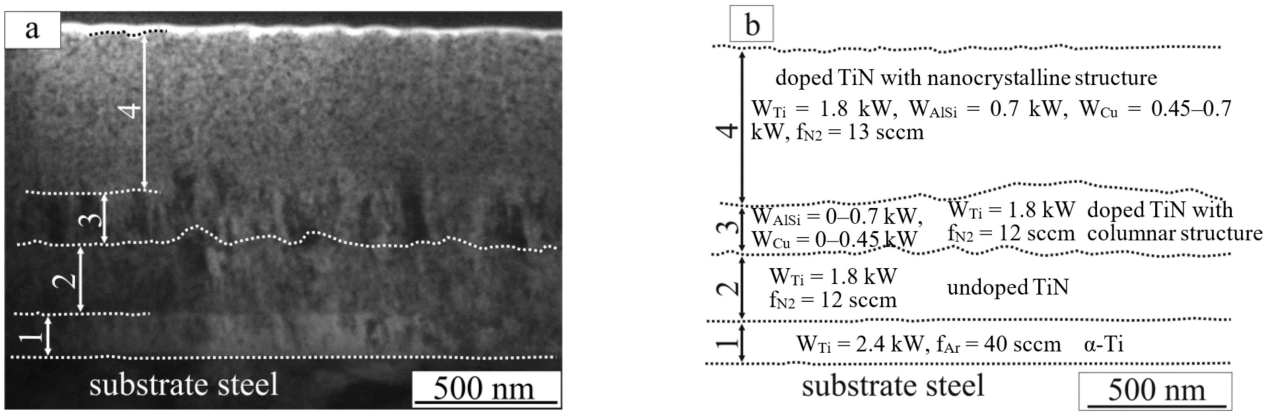

Figure 2. The bright-field image (**a**) of the structure of the gradient-laminated Ti-Al-Si-Cu-N coating and its scheme (**b**). Notation for (**a**): 1—α-Ti sublayer, 2—layer of non-alloyed TiN, 3—layer of alloyed TiN, 4—layer of alloyed TiN with nanocrystalline structure. Notation for (**b**): W—the power of the sputtering specific target, f—gas flow.

Such a structural peculiarity, like other smaller structural characteristics of coating growth, was conditioned by altering the concentrations of alloying elements throughout the thickness and calculated using the spectra of the characteristic X-ray radiation (Figure 3a). According to the plots in Figure 3b,c reflecting the concentrations of separate elements, both the general and specific characters of their change could be identified. In particular, the alteration of the silicon and aluminum concentrations was specific due to their relatively fast growth in the layer with a columnar structure, up to a distance of 430 nm from the α-Ti sublayer, which also corresponded to the time interval of the $Al_{60}Si_{40}$ target sputtering power increase. However, their smaller but evident increase in the nanocrystalline region (whose growth was accompanied by an almost two-fold increase in copper target sputtering

power only), could be conditioned only by the peculiarities in the phase formation in the nanocrystalline structure of this system of elements.

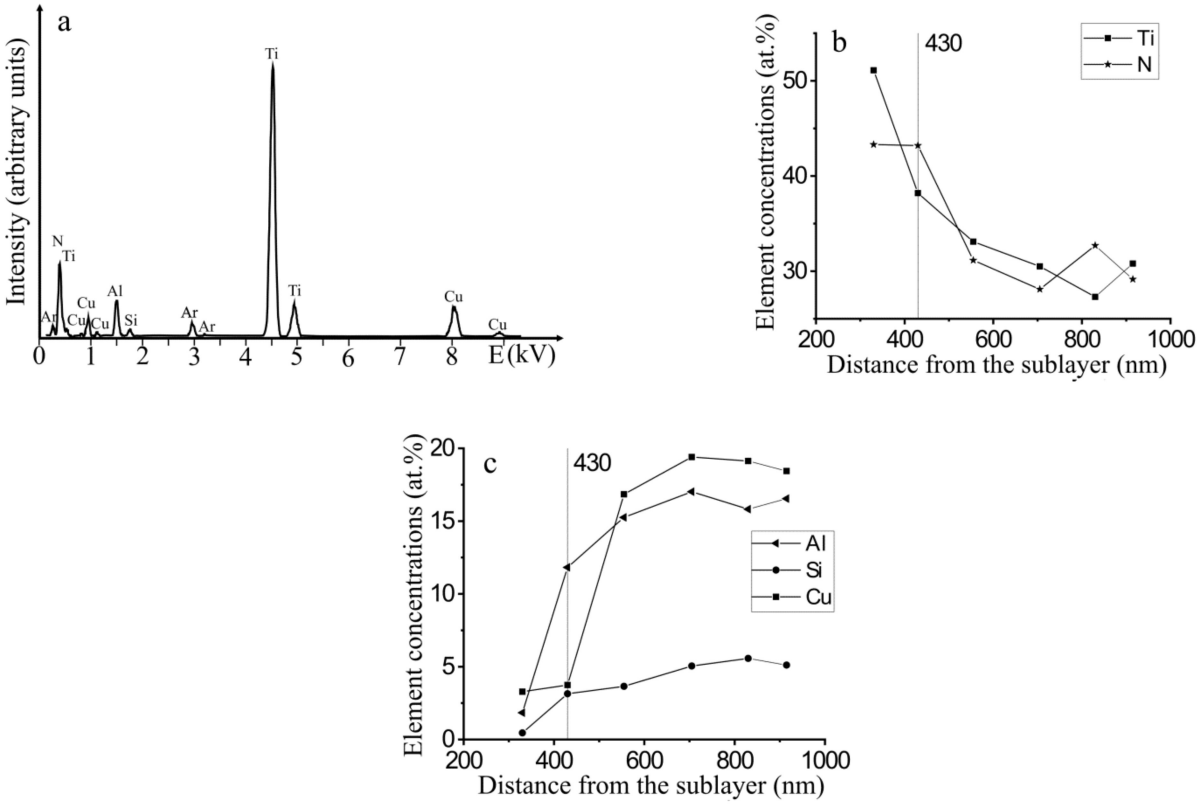

Figure 3. The elemental composition of the gradient-laminated Ti-Al-Si-Cu-N coating. (**a**) Characteristic X-ray spectrum at a point near the interface between the nanocrystalline and columnar layers; (**b**,**c**) plots of element concentration in the coating vs. distance from the α-Ti sublayer.

The increased growth in the concentrations of the alloying elements (Al, Si, Cu) in the nanocrystalline region caused a sharp decrease in the nitrogen and titanium concentrations in this region (by ≈13 and 10 at.%, respectively). Since the phase composition of the nanocrystalline region was alloyed FCC titanium nitride and copper, it should be assumed that an increase in the copper concentration on the growth surface reduced the efficiency of the titanium nitride phase nucleation. This effect was possible due to the low bonding energy in Cu-N, which caused the decreased concentration of nitrogen in the coating [17], and hence, the increase in the time interval for the formation of nucleation crystals and instability of the nitride phase.

The latter will affect the intensity of the secondary sputtering of elements from the coating surface, in particular, by increasing the sputtering efficacy of titanium atoms that are more weakly bonded in nonstoichiometric nitride, which should decrease its concentration. The elements alloying nonequilibrium TiN nitride also experience sputtering from the growing coating surface. We should note, for example, that the efficacy of secondary sputtering manifests in the lower (virtually halved) concentration of Si in the nanocrystalline layer as compared to the gradient coating of the same composition, but was obtained at a 1.5-fold lower bias potential on the substrate [18]. However, such results demonstrate that their position in the lattice or along the boundaries of growing crystals (on which Si segregates [1]) turned out to be more resistant to sputtering.

The interpretation of electron microdiffraction images of different sections of the coating unveiled, first, that in the coupling region of the α-Ti sublayer, there was parallelism of certain crystallographic planes of γ-Fe and α-Ti (denoted by arrows in Figure 4a). This testified to a certain minimization of the interaction energy in the "surface–substrate" system, i.e., minimization of stress relaxation expressed as azimuthal blurring of γ-Fe

reflexes in Figure 4a, and can positively affect the adhesive properties of the sublayer. Second, the phase composition of the coating changed throughout its thickness (see reflexes on separate phases in Figure 4b,c):

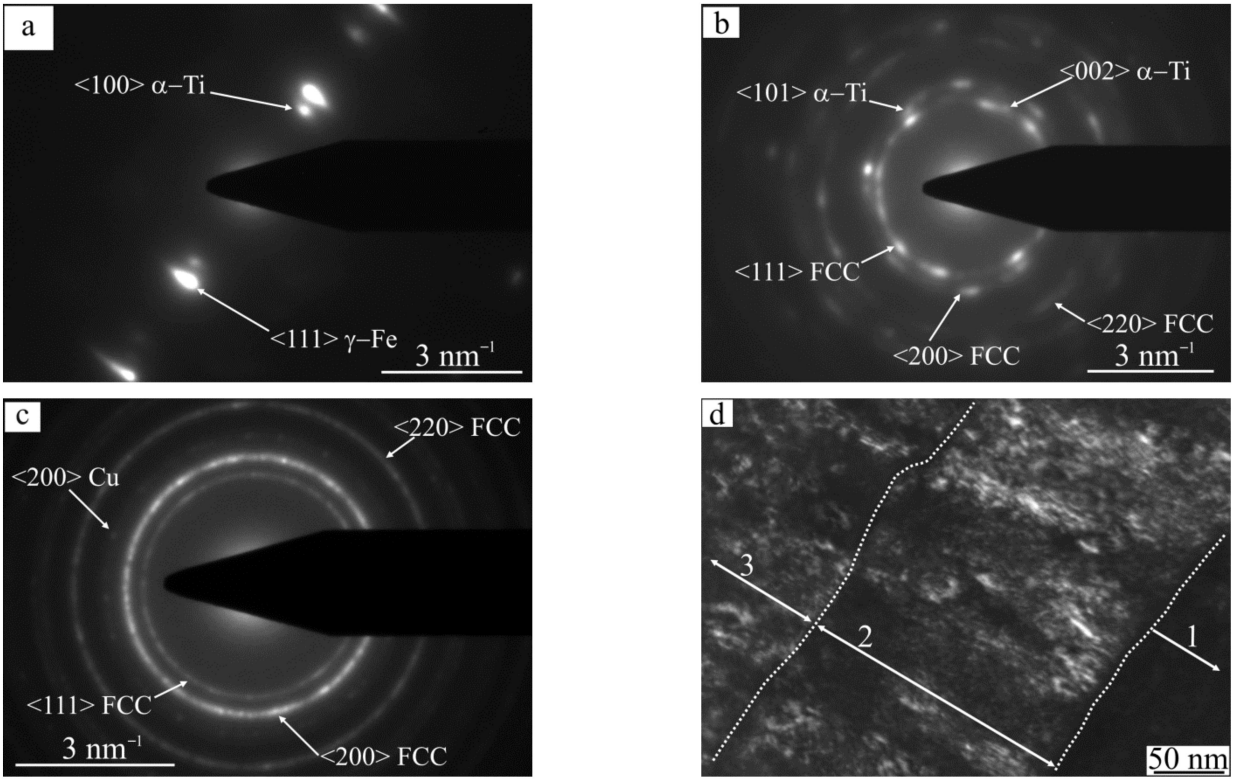

Figure 4. Microdiffraction electron patterns for the different coating layers (**a**–**c**) and the dark-field image (**d**) of columnar coating structure in reflexes <111> and <200> of TiN nitride (see notation in Figure 2a).

The presence of α-Ti particles in the upper part of the submicrocrystalline layer evidently testified to the lack of nitrogen due to the aforementioned influence of copper and excess of Al that were soluble in metastable conditions of the coating synthesis in the metal sublattice [19].

At its higher concentrations in the nanocrystalline state, copper was liberated as separate crystals (Figure 4c). The lattice parameter of the nitride phase calculated for the submicrocrystalline and nanocrystalline regions showed that its value monotonically dropped in the alloyed nitride when approaching the coating surface from ≈0.425 ± 0.001 nm to ≈0.418 ± 0.001 nm. The largest drop (by ≈0.004 nm) was recorded for the submicrocrystalline region, which could have been conditioned by the effect of the alloying or substoichiometric amount of nitrogen (compare Figure 4b,c). Such a result qualitatively coincided with that in [19,20] in terms of the decreasing lattice spacing in titanium nitride after the dissolution of aluminum and silicon.

The diffraction patterns of the submicrocrystalline columnar structure showed no pronounced texture. However, the dark-field image in reflections <111> and <200> (Figure 4d) demonstrated that the planes that corresponded to those reflections in the majority of columnar grains with a diameter of 20–90 nm were in reflecting positions, which may testify to the 60° rotation of the crystal lattice around direction <110>, which is common for the said planes at adjacent large-angle boundaries.

The investigation of crystal lattice bending–torsion in different layers of the coating demonstrated that it was relatively small for the submicrocrystalline structure of non-alloyed titanium nitride: the component χ_{21} of the bending–torsion tensor averaged ≈35° μm^{-1}. However, the same component in the layer of alloyed titanium nitride was

considerably higher and averaged ≈85° μm^{-1}. Figure 5a,b illustrates the determination of crystal lattice bending in the last layer. It is shown that the extinction contour (denoted by the dotted line) on inclination was displaced differently in different directions, which testified to the anisotropy of the crystal lattice bending–torsion values in the structure of the columnar crystal. In particular, in the directions r_1, r_2 and r_3, such displacements amounted to 3.3, 6.8 and 4.8 nm, respectively. Since in this case, angle β in Equation (1) was ≈60° and φ ≈ 0.5°, the data on the contour displacement reflected the values of component χ_{21} ≈ 130, 65 and 90° μm^{-1}, correspondingly.

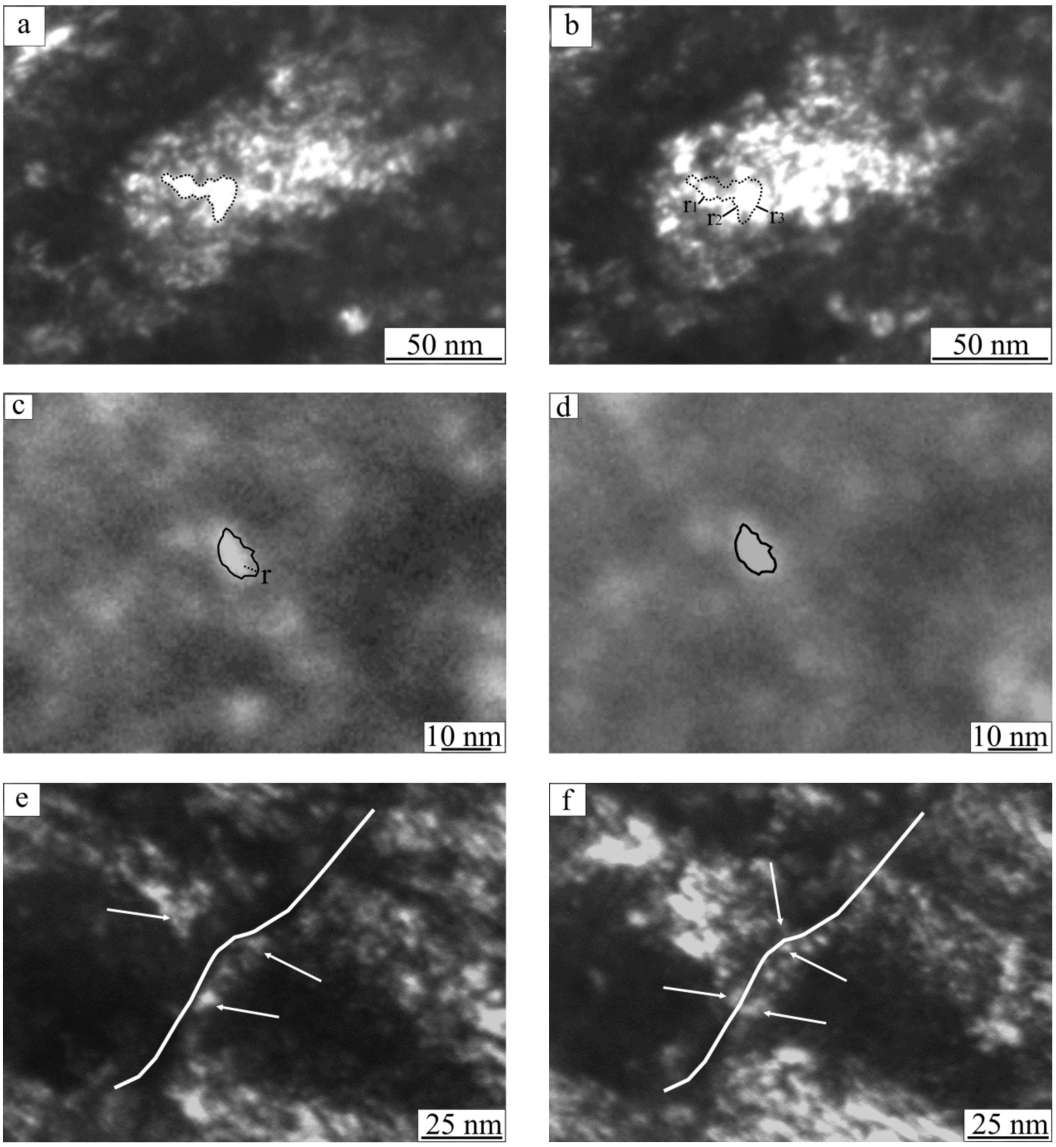

Figure 5. Dark-field images of bending extinction contour displacement characterizing the bending of the crystal lattice in columnar (**a**,**b**) and nanocrystalline (**c**,**d**) structures and misorientation of the reflecting planes of <220> type at the boundary of the alloyed and non-alloyed nitride (**e**,**f**) (lines and arrows denote extinction contours; their displacements are denoted by lines with letters; the boundaries in (**e**) and (**f**) are denoted by a white line).

The largest average crystal lattice bending (≈115° μm^{-1}) was reached in the nanocrystalline layer with its alteration range of 50–190° μm^{-1}. Figure 5c,d depicts the examples of a nanocrystal with high crystal lattice bending. A similar calculation using Equation (1) with the parameters of r ≈ 3.0 nm, β ≈ 70° and φ ≈ 0.5° yielded χ_{21} ≈ 156° μm^{-1}. Moreover, the application of the dark-field method for analyzing misorientations in prolonged layer

interfaces demonstrated that the boundary occurring at the low alloying degree of TiN (boundary between layers 2 and 3 in Figure 4d) was a small angle, which is illustrated in Figure 5e,f. Evidently, from Figure 5e, the extinction contour above the boundary (shown as the dark line) was several dozens of nanometers from it, while below the boundary, the contour was located near the boundary (arrows in Figure 5e). With a 1° inclination, the extinction contour above the boundary was immediately adjacent to it (Figure 5f). Therefore, one of the horizontal components of the misorientation vector was at the boundary ≈1°, which testified to its small angle. At a high TiN alloying degree, the boundary between layers with different structures had a large angle, which correlated with the alteration of the coating growth mechanism.

3.2. Hardness and Structure of Coatings in Indentation Zones

The deformation behavior of the coating–substrate system was studied over a load range of 5–400 mN. The coating hardness was estimated at the lowest load of 5 mN when the maximum indenter penetration depth amounted to about 10% of the coating thickness (Figure 6a). In this case, when the effect of the substrate on the coating hardness could be neglected, its value was determined by the elastoplastic properties of the coating itself. In particular, the value of relaxation creep (the ratio of the displacement value at maximum load to the total indent depth) could reach 3.3%, while the value of the elastic return of the maximum indent depth did not exceed 50%. Since after unloading in this case, the distance between the load–unload curves only increased and the indent depth was several times smaller than the nanocrystalline layer thickness, the behavior of its heterophase structure was plastic. The average hardness was ≈16 GPa, with the scatter of the value ranging from 15 to 18.5 GPa.

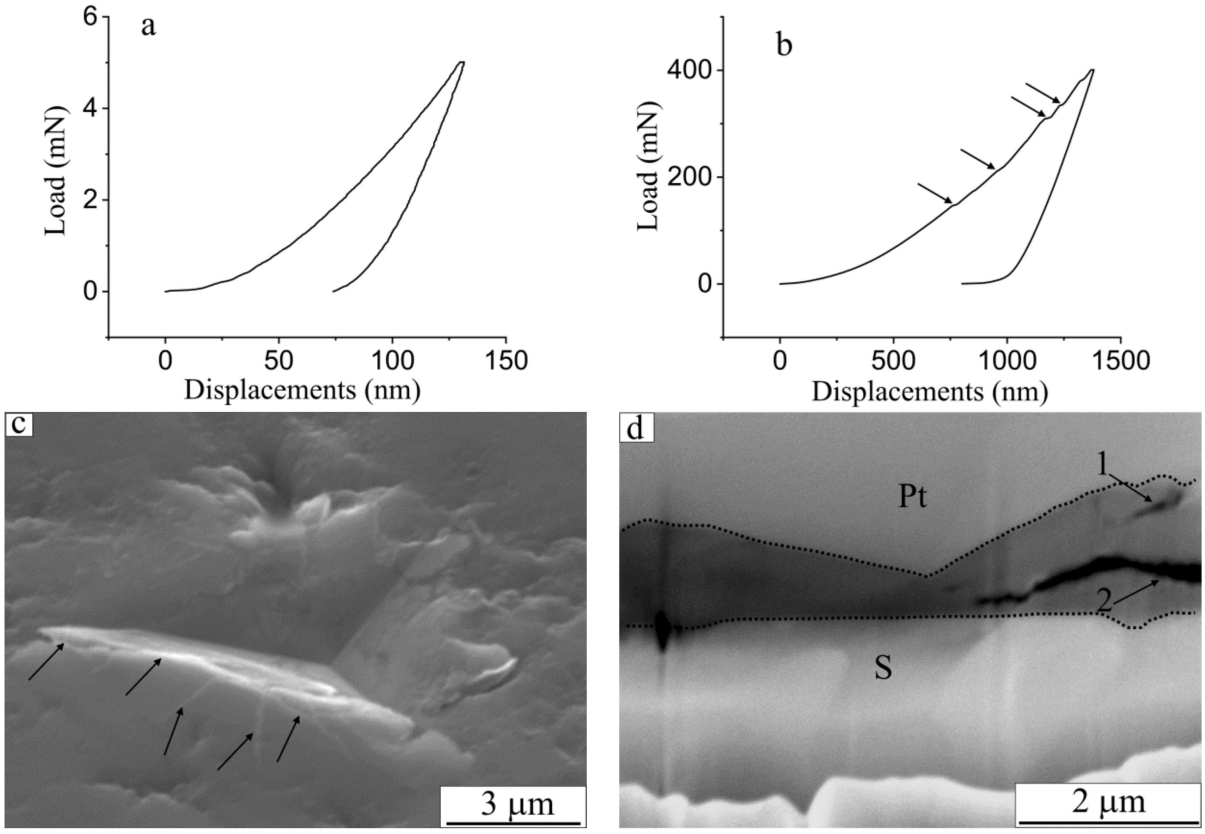

Figure 6. Load–displacement curves for indentation with different depths of maximum indenter penetration (**a**,**b**) and images (scanning microscopy) of indents in the coating plane (**c**) and coating cross-section (**d**). Notations in (**d**): S—substrate (T15K6 alloy), 1—inclined cracks on the indent's ridges, 2—cracks throughout the interface between the layers.

When increasing the load to 140–160 mN (corresponding to the maximum indenter's penetration depth of 700–750 nm), the loading curve changed smoothly without irregularities, while at large loads, the curves demonstrated inflections and plateaus that corresponded to the intensification of the deformation and fracturing (arrows in Figure 6b). In this case, scanning microscopy of the indentation surface showed cracking and formation of the relief along the ridges of the indents (Figure 6c), while there were no cracks on the indent faces closer to the tip. This result was also confirmed by the indent cross-sections (Figure 6d), which showed no cracks reaching the coating surface. This means that in the central part of the indent in the vicinity of the surface, the plasticity and homogeneity of the nanocrystalline layer structure—along with compressing stresses under the tip—provided both stress relaxation in the crack tips and a power barrier preventing their evolution.

The origins of large cracks were zones of bending stress concentration at the indent ridges [21] (arrow 1, Figure 6d), interfaces between coating layers (arrow 2, Figure 6d) and—on very rare occasions—the interface between the coating and α-Ti layer. Thus, we should note that possible fracture factors along the interface between the alloyed and non-alloyed titanium nitride may have been the difference in their plastic properties and stress concentration on a prolonged defect that initiated the origination and merger of cracks along it. The merger and opening of such cracks were promoted by the plastic flow of the material in the indent in the perpendicular direction to the loading axis and by the relaxation of elastic compression stresses on unloading. On the other hand, it was evident that maximum compression stresses under the tip prevented the formation of such cracks under loading.

Transmission electron microscopy of this section (Figure 7a) showed that the substrate surface near the indent remained flat, i.e., there were no displacements along the boundaries of columnar crystals or radial cracks along these boundaries in the region of coating coupling with the substrate. Therefore, the correlation of the properties of the coating and substrate (T15K6 alloy) determined the absorption of indentation energy due to the plasticity and fracturing of the coating in the first place.

We should note that in the nanocrystalline layer, there were no single large straight cracks. However, there were separate fracture areas (voids with dimensions of up to ≈40 nm, Figure 7b, arrows 1), between which, there were separate curvy nanosized (up to ≈30 nm in length) regions of lower width (therefore, they were brighter in the bright-field image) that could be interpreted as cross-section regions with cracks. Hence, the fracture mechanism in such a nanocrystalline structure had multiple stages, and fracturing was prevented by the evolution of multiple dendritic cracks.

Moreover, in certain regions under the indenter's tip near the interface between the nanocrystalline layer and columnar layer, the latter contained separate nanosized (≈30–40 nm long and ≈2–3 nm wide) thinner regions that were similar to those above (thus being brighter in the bright-field image, arrows 2 in Figure 7b) and inclined to the loading axis. Based on this and due to the linear morphology of such regions, a similar characteristic distance between them (20–25 nm) and the diameter of the columnar structure grains, we could hypothesize that these were the cracks that evolved along former boundaries of the columnar structure.

Together with the cracks, the dimensions and shape of the indents were determined using macroscopic plastic deformation of separate coating layers. The evident measure of such a deformation (ε(r))—due to the virtually absent deflection of the substrate—is the ratio of coating layer thickness in the indent region to its value (h_0) after the coating deposition, i.e., $\varepsilon(r) = (h(r) - h_0)/h_0$, where h(r) is the layer thickness at distance r from the indenter's tip. Such measurements of the thickness of different layers are partially shown in Figure 7c; the calculations of the deformation values ε(r) are given in Table 1.

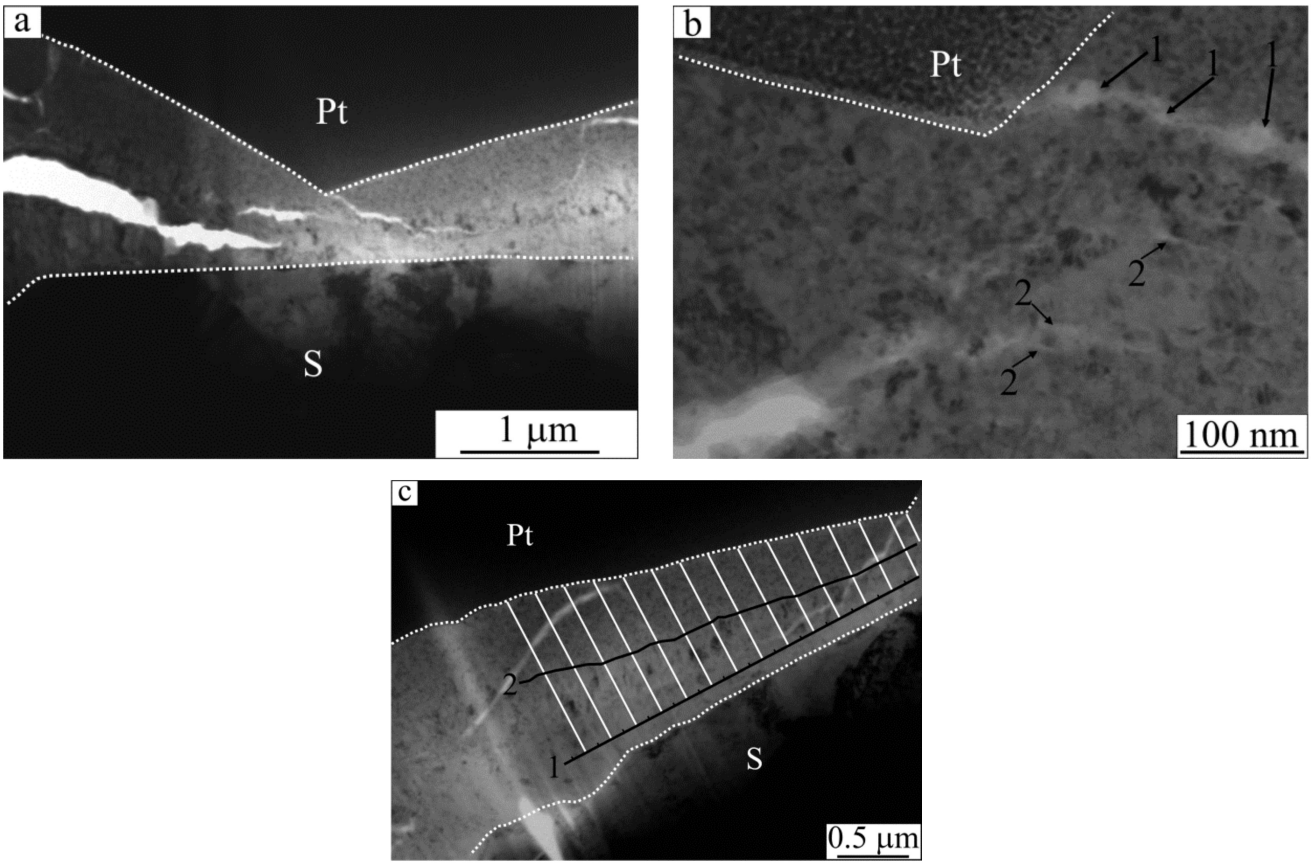

Figure 7. Bright-field image of the structure in the transverse cross-section of the indent. (**a**) General view. (**b**) Zoomed-in image of the region under the indenter's tip; notations: 1—areas of fracture in nanocrystalline layer, 2—nanosized cracks. (**c**) Zoomed-in image of the indenter face; notations: 1—upper boundary of α-Ti layer, 2—upper boundary of columnar layer, S—substrate.

Table 1. Values of coating layer deformation (%), which depend on the distance R from the indenter's tip.

R (nm)	Nanocrystalline Layer	Columnar Layers	R (nm)	Nanocrystalline Layer	Columnar Layers
0	53	-	1500	−0.8	15.1
100	42	57	1700	−6.6	12.7
300	31	54	1900	−11.6	3.5
500	20.4	53.5	2100	−22.2	0
700	16	45.5	2300	−29.5	−6.7
900	9.2	41	2500	−25.5	−23.5
1100	5.7	31	2700	−21	−35
1300	1.3	21.8	-	-	-

These calculations were undertaken using the most probable thicknesses of the nanocrystalline layer and columnar layer after deposition on the T15K6 hard alloy and amounted to ≈455 nm and ≈450 nm, respectively. First, we should note that these data were approximate because, in the indent zone of the majority of regions, there was no pronounced interface between the columnar layer and α-Ti sublayer. Therefore, the interface between them was denoted based on the data on the sublayer thickness after deposition.

However, the image in the sublayer of the separate columnar crystals of the TiN and α-Ti below, down to the interface with the substrate, allowed for making an approximate assessment of its thickness of ≈130 nm. This is why the alteration of the thickness, as compared to the state after deposition (Figure 2a), amounted to about 10–15 nm, while

the estimated measurement error (the positive one) of deformation amounted to ≈2–3%. Moreover, a certain measurement error was due to cracks in the layers. Second, the interface between the columnar layers of the alloyed and non-alloyed titanium nitride could not also be identified (Figure 7c); therefore, the combined deformation for these two layers is presented. However, it is evident that there should be a distribution of plastic deformation between the layers due to the difference in their elastoplastic properties.

Third, the deformation of both layers amounted to dozens of percent, and more in magnitude, especially with increasing distance to the tip, in the case of the layer with columnar structure. In addition, as follows from Figure 7c, the residual indent depth was smaller than the nanocrystalline layer thickness after deposition. Hence, the nanocrystalline layer was the main load-bearing layer because it had higher stiffness, i.e., restoration capability after load relief. Fourth, the deformation value throughout the indent cross-section had different signs for both layers (Table 1), which testified to the mass transfer at the scale of the indent in the direction normal to the loading axis.

Following the known data regarding the somewhat higher hardness of the substrate vs. that of the coating (≈18 GPa vs. ≈15.6 GPa) and its reduction down to an average value of ≈12.8 GPa with the increase of the load to 100–150 mN (and indent depth to 700–900 nm), we suggest that the relatively high deformation of the columnar layer may have been a consequence of a specific deformation of a softer columnar layer between two stiffer and harder layers: the substrate and nanocrystalline layer. Larger dimensions of the compression deformation zone and its larger value for the columnar layer could have been conditioned by the limiting effect of the upper layer deformation on unloading and the dimensional effect of the deformation zone enlargement with increased depth (distance from the indenter's tip). However, the structural mechanisms of mass transfer and the resulting peculiarities of the microstructure should vary due to the different initial structures of the coating layers. Therefore, let us consider the peculiarities of the defect microstructure of the layers in the indentation zone.

First of all, we should note that in the submicrocrystalline region, the deformational alterations of the structure under the tip were expressed as the fracture of the columnar structure due to the formation of a multitude of interfaces that were transverse to the growth direction (noted by white arrows in Figure 8a and arrows 2 in Figure 8b). This led to the formation of an equiaxial crystalline structure in this region with crystal dimensions of up to 100 nm. Evidently, in this case, the boundaries were of deformational origin. Moreover, near the tip on the side faces of the indent, the columnar crystals were inclined; therefore, their direction remained virtually perpendicular to the indent faces (arrows 1 in Figure 8b and dotted lines in the lower part of Figure 8c).

The formation of large cracks on the indent face along the interface between alloyed and non-alloyed titanium nitride (Figure 8c) expectedly demonstrates the stress relaxation and cessation of the deformational mechanism of columnar boundary inclination. According to the upper part of Figure 8c, the direction of columnar grain boundaries (dotted lines) in the non-alloyed titanium nitride was perpendicular to the substrate, i.e., it did not change with indentation. Thus, these data and the results of the investigation of alterations in the columnar structure boundary characteristics in monolayer coatings [22] showed that, with compression under the indenter's tip, the boundaries that were transverse and inclined to the compression direction effectively relaxed the stresses in this region.

Figure 9a,b depicts microdiffraction images of the structure under the indenter's tip. Obviously, at a relatively small fraction of the columnar structure (less than 10%), under the selector diaphragm, the texture orientation was weakly pronounced. Actually, prolonged segments of quasi-ring reflexes of increased intensity could be identified only on reflections of <220> type (arrows 1 in Figure 9a). For other reflections (<111> and <200>), the nonuniformity of the structure was expressed in separate bright reflections, the position of the majority of which (e.g., on reflection <200>) could not be correlated with said texture reflections. Concurrently, in the state after the depositions, the diffraction pattern of the nanocrystalline layer had a more uniform reflection intensity (Figure 4c). This

is why this specificity of microdiffraction could reflect the growth of nanocrystals under the indenter's tip.

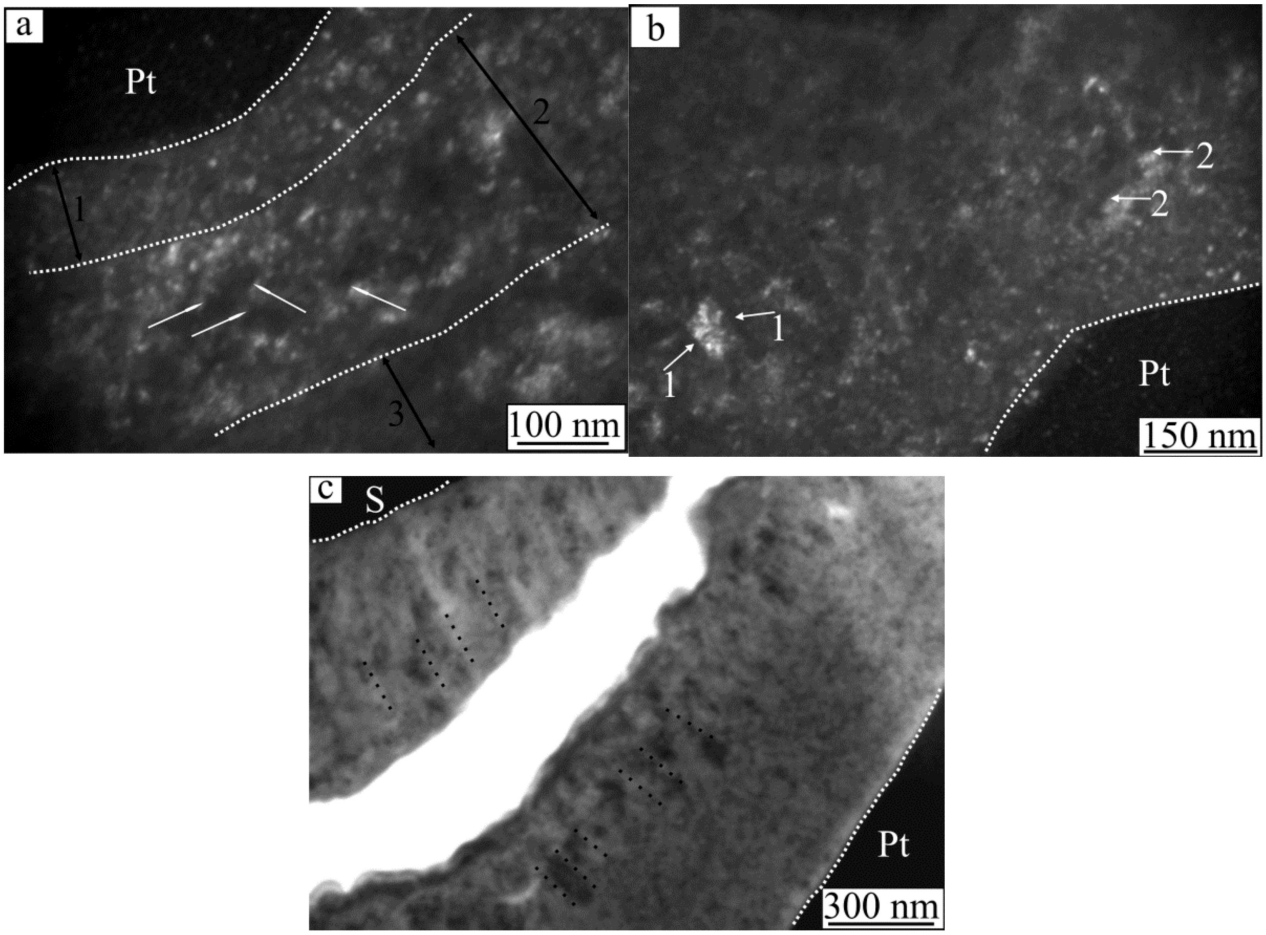

Figure 8. Dark-field (**a**,**b**) and bright-field (**c**) images of the microstructure in the indented region. Notations in (**a**): 1—nanocrystalline layer, 2—columnar layer, 3—α-Ti sublayer. Notations in (**b**): 1—inclined boundaries of columnar grains, 2—misorientation boundaries that are perpendicular to the loading axis. Notations in (**c**): S—substrate, dotted lines denote the boundaries of columnar crystals in different parts of the coating.

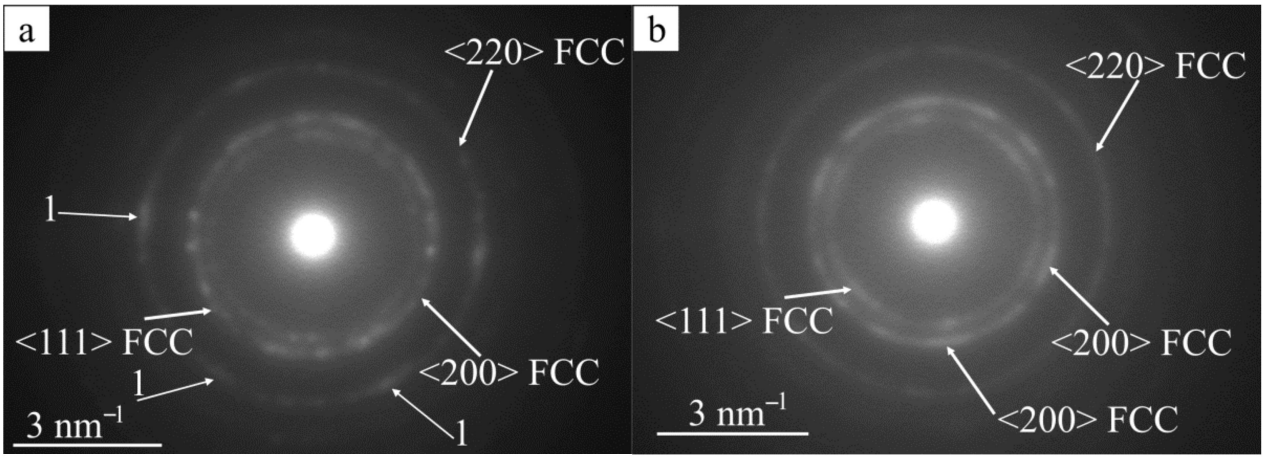

Figure 9. Electron microdiffraction patterns from different regions under the indenter's tip: (**a**) from the nanocrystalline layer; (**b**) from the columnar layer.

Therefore, in the dark-field images of the nanocrystalline structure after the deposition, the dimensions of crystals (regions of coherent scattering) were measured (about 100 measurements for each direction) in the directions parallel and perpendicular to the loading axis. It was established that for the latter direction, both the average and maximum dimensions of crystals under the tip increased by almost 40% and reached 9.3 and 22 nm, respectively. In the direction of the loading axis, the dimensions of crystals remained almost unchanged; for instance, they averaged ≈7.2 nm.

Such an increase in crystal dimensions, from the perspective of the assessment method, corresponds to decreased bending in crystal planes of the lattice that are perpendicular to the loading axis. Such a decrease, according to the loading scheme, can follow from compression stresses under the indenter's tip. Furthermore, shear stresses provide macrodeformation and, probably, grain-boundary creep of nanocrystals, which are capable of forming shear stresses in them that are perpendicular to the loading axis. In the presence of separate defects in crystals that generate fragmentation (for example, dislocations), they can be displaced to boundaries by the stresses, which should increase the coherent scattering region dimensions in the noted direction.

Another discrepancy in the diffraction from below the indenter's tip was the absence of reflections from the copper phase (Figure 9a) that were identified in the nanocrystalline layer under the indent faces. More ambiguous were the data on the phase composition of the submicrocrystalline layer under the tip in which α-Ti particles were identified for some of the indents (not shown). With increasing distance from the tip, the microdiffraction pattern started to demonstrate texture orientation components (arrows in Figure 9b for reflection <200>). In general, the uniformity of the reflection intensity was higher than that in the state after deposition for both the separate quasi-ring reflections and the pairs of different reflections (compare those in Figure 4b). For example, in the latter case, the ratio of intensities of reflections <200> or <110> to the same value of <220> amounted to 200%, but only to ≈150% under the indenter's tip. Evidently, this testified to the dispersion of the structure in the bulk of columnar crystals. Therefore, the microdiffraction patterns qualitatively demonstrated the opposite behavior of the structural alteration in different layers under the indenter's tip.

The calculations of electronograms shown in Figure 9a,b demonstrated that under the tip in the zone of the most intense deformation, the crystal lattice parameter of alloyed titanium nitride in the nanocrystalline and columnar layers leveled out and amounted to $d^a \approx 0.416 \pm 0.001$ nm. Consequently, the microdeformation of the lattice associated with this change was higher in the layer of the columnar structure.

This could be estimated using the known crystal lattice parameter ($d^{in} \approx 0.420 \pm 0.001$ nm) at the interface between nanocrystalline and submicrocrystalline layers because it was the very region the microdiffraction patterns, such as that presented in Figure 9b, were obtained. Following the assumption regarding the constancy of the elemental composition in this region, the lattice microdeformation (ε^M) in it will be equal to $\varepsilon^M = \left(d^{in} - d^a\right)/d^{in}$, i.e., remain in a range of ≈0.5–1.2%, which testified to the redistribution of structure defects under the indent tip and formation of a compression stress state in microvolumes of ≈E/200—E/100, where E is Young's modulus of the coatings.

Noted nonuniformity of microdeformation in different layers of the coating follows from its similar behavior at a smaller scale (local deformation for the size of separate crystals), which can be determined using dark-field analysis of crystal lattice bending–torsion. In terms of the nanocrystalline structure under the indenter's tip, the application of this method is illustrated in Figure 10a,b. Following the comparison of extinction contour positions (enclosed by the solid line in Figure 10b), with an inclination of ≈0.5°, it displaced to a distance r ≈ 4 nm. After substituting these values into Equation (1), we obtained a value of the bending–torsion tensor component χ_{21} of ≈125° μm^{-1}, which, according to the statistics of several dozens of similar assessments, is an average value of a nanocrystalline layer under an indenter's tip.

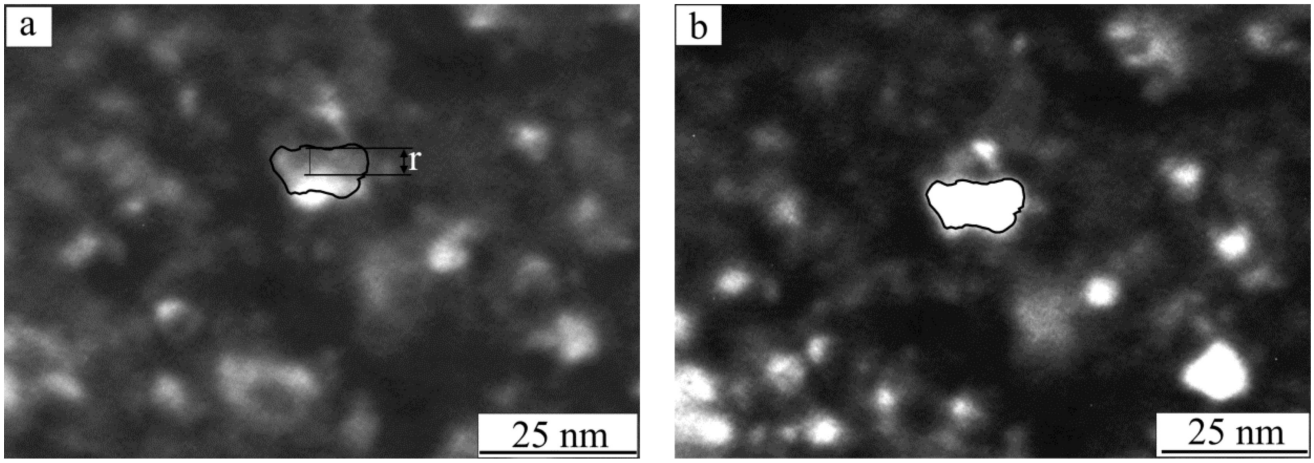

Figure 10. Dark-field images of extinction contour displacement in a nanocrystalline region under the indenter's tip with foil inclination: (**a**) sample tilt angle 0°, (**b**) sample tilt angle 0.5° (see explanation in text).

The comparison of this parameter for the state after deposition showed that the increase in component χ_{21} in the indent region was small (≈10% of the initial value of 115° μm^{-1}) and that its alteration range was almost the same ≈55–180° μm^{-1} (without taking into account the near-boundary regions of the crystal, see below). A more significant difference was the reduction in the most probable value of χ_{21} near the indentation zone (as compared to the initial state) by 30% down to ≈100° μm^{-1}. The combination of these data showed certain "polarization" of the crystals in terms of the crystal lattice bending–torsion value: on the one hand, a drop in the level of deformations and stresses for a prevailing fraction of nanocrystals; on the other hand, the increase in the fraction of crystals with a higher bending–torsion tensor component value as compared to the state after deposition.

In particular, while after the deposition, the fraction of crystals with χ_{21} > 150° μm^{-1} was ≈10%, this value was 40% in the indent zone under the tip. Evidently, these results reflected the correlation of the active and relaxation fractions of the deformation due to indentation and nonuniformity of deformation at the nanoscale (below 100 nm) since, in general, such an alteration of component χ_{21} was also found in other regions of the indent (not only under the tip).

Based on this, we should note the manifestation of the stress relaxation effect (crystal lattice bending) expressed as the formation of dipole configurations of the misorientation of nanocrystal volumes. An example of such a configuration is given in Figure 11. For instance, in Figure 11a, the extinction contour passed through all of cross-section 1–1 of the crystal at a foil inclination angle of ≈0°. At an inclination of the specimen of 0.5°, the contour in the central part of the crystal disappeared, while at the periphery, it remained, though with a lower intensity (Figure 11b). Hence, the reflecting planes of the <220> type at the crystal center were misoriented in relation to the peripheral planes, while the latter were oriented parallel to each other. This is why in cross-section 1–1 at the boundaries of the peripheral regions (indicated by dotted lines in Figure 11b), there were rotations of reflecting planes in opposite directions, i.e., their dipole configuration.

Qualitatively similar behavior was observed in cross-section 2–2 of the crystal in Figure 11b,c: the extinction contours at the periphery of the crystal (Figure 11b) faded away at an inclination of 0.5°, while in the central part of the crystal, the planes came to the reflecting position (Figure 11c). We should also note the following regarding the aforementioned cross-sections. First, for cross-section 1–1, the peripheral contour of the crystal remained for a larger angle range as compared to the central part, i.e., the reflecting planes in these regions were more bent in the direction of the electron beam propagation (this bending corresponds to component χ_{31} of the lattice bending–torsion tensor) because,

with inclination, separate segments of these planes moved into a reflecting position (see details in [15]).

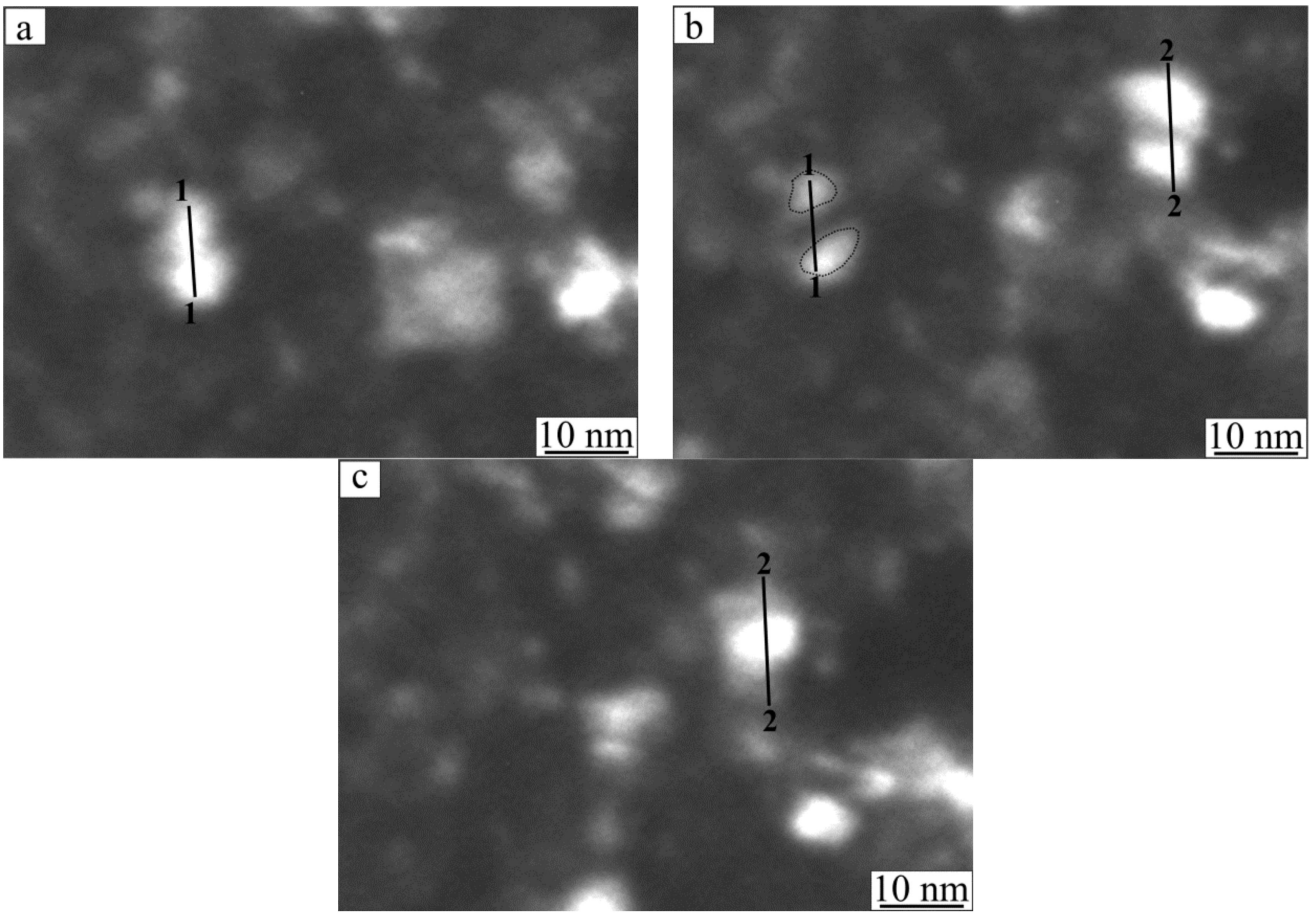

Figure 11. Dark-field images of displacement of bending extinction contours in crystals that illustrated the nonuniformity and multi-dimensional character of the orientation switch for reflecting planes, (**a**) sample tilt angle 0°, (**b**) sample tilt angle 0.5°, (**c**) sample tilt angle 1° (see explanation in text).

Second, in cross-section 2–2, the boundaries of extinction contours in the center (Figure 11c) and at the periphery (Figure 11b) did not precisely coincide; they partly overlapped. Such an alteration of the contour position also testified to the presence and nonuniformity of the bending of reflecting planes, which was connected with the noted component χ_{31} of the bending–torsion tensor. Hence, these data demonstrated the formation of a multi-dimensional bending of the crystal lattice of nanocrystals under the indenter's tip.

When investigating the peculiarities of the crystal lattice bending–torsion, one should note a structure state near the boundaries of the crystals. Such regions were characterized by higher (2–4-fold) values of the lattice bending–torsion as compared to the noted average value. For instance, Figure 12a,b shows that at an inclination of 0.5°, the extinction contour (denoted by the dark line) displaced to a distance of r ≈ 1.5 nm toward the upper crystal boundary (faded away at a larger inclination). According to Equation (1), such a displacement corresponded to $\chi_{21} \approx 330°\ \mu m^{-1}$. However, near adjacent boundaries, the contour remained, which was conditioned (according to the above) by the presence of a non-zero χ_{31} component.

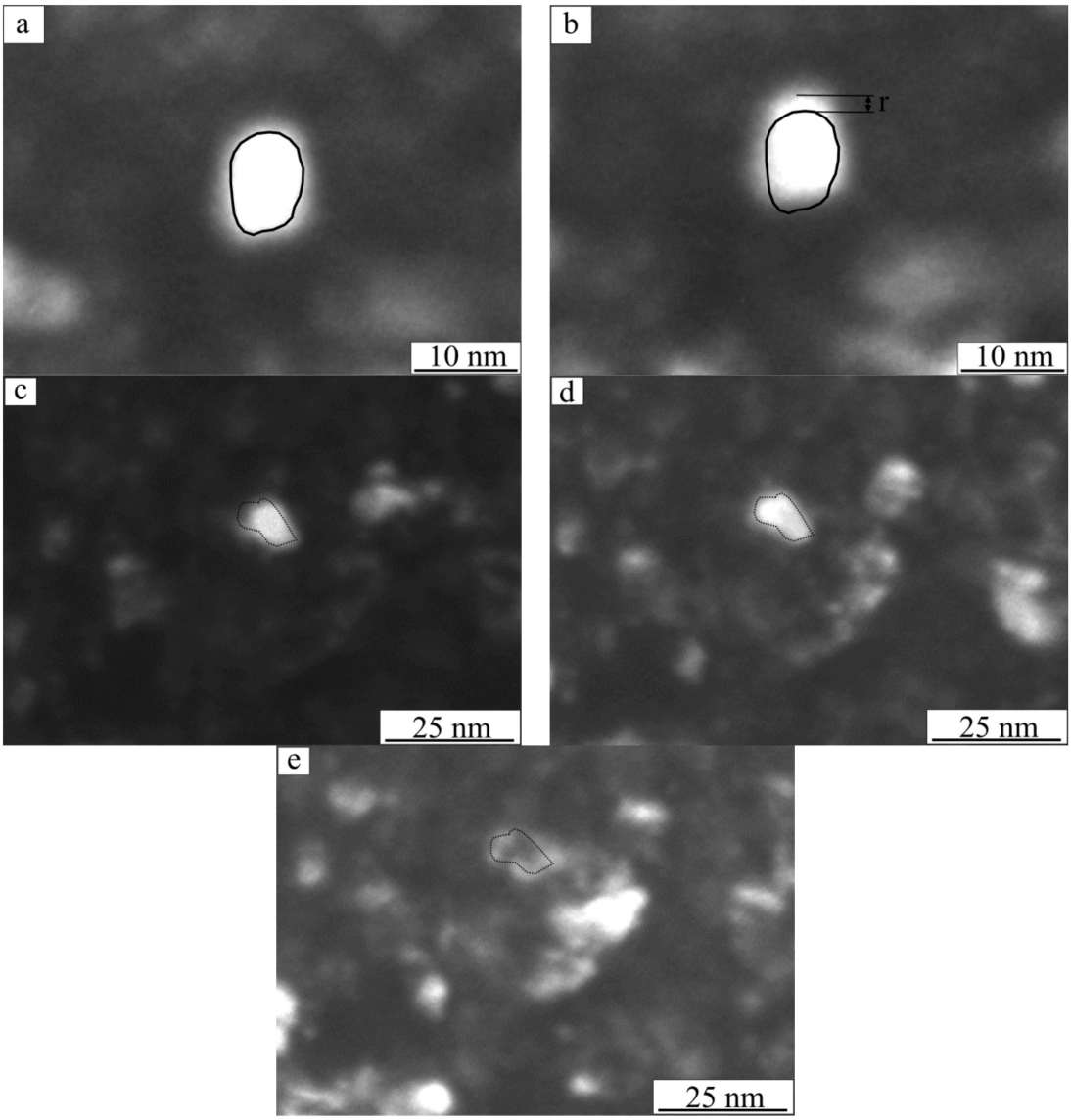

Figure 12. Dark-field images of extinction contour movement that reflected the high values and nonuniformity of crystal lattice bending near the crystal boundaries (**a**,**b**: **a**—sample tilt angle 0°, **b**—sample tilt angle 0.5°) and misorientation of the central and periphery of the crystals (**c**–**e**: **c**—sample angle tilt 0°, **d**—sample angle tilt 0.5°, **e**—sample angle tilt 1°) (see explanation in text).

The misorientation of the center and periphery of the crystals was typical, as exemplified in Figure 12c–e. It is shown that with the inclination of the specimen, the first to come into reflecting position were planes of the <220> type in the center of the crystal (Figure 12c, the crystal is denoted by the dotted line), while at larger inclination angles (Figure 12d,e), the first were those at the periphery. In this case, there was a nonuniformity of χ_{31} along the boundaries because the contour, though being of low intensity, was not detected along the whole dotted line enclosing the crystal boundary (Figure 12e). Therefore, such results reflected the role of grain boundaries as a source of elastic deformations (stresses) and nonuniformity of their values at scales less than the crystal dimensions.

The investigation of the crystal lattice bending–torsion in the layer with initial submicrocrystalline columnar structure under the indenter's tip showed a negligible (as compared to the initial state) increase in its average value up to $\approx 100^\circ$ μm^{-1} within a range of 55–130° μm^{-1}. These data on the alterations were qualitatively and quantitatively close to the bending alteration in the nanocrystalline layer.

Dark-field TEM images of the microstructure under the indenter's tip in the former zone of the columnar crystals (presented in Figure 13) showed the fragmentation of relatively large non-equiaxial subgrains (two boundaries of one of them are denoted by the dotted lines) into nanosized fragments (crystals, coherent scattering regions) with dimensions of several nanometers.

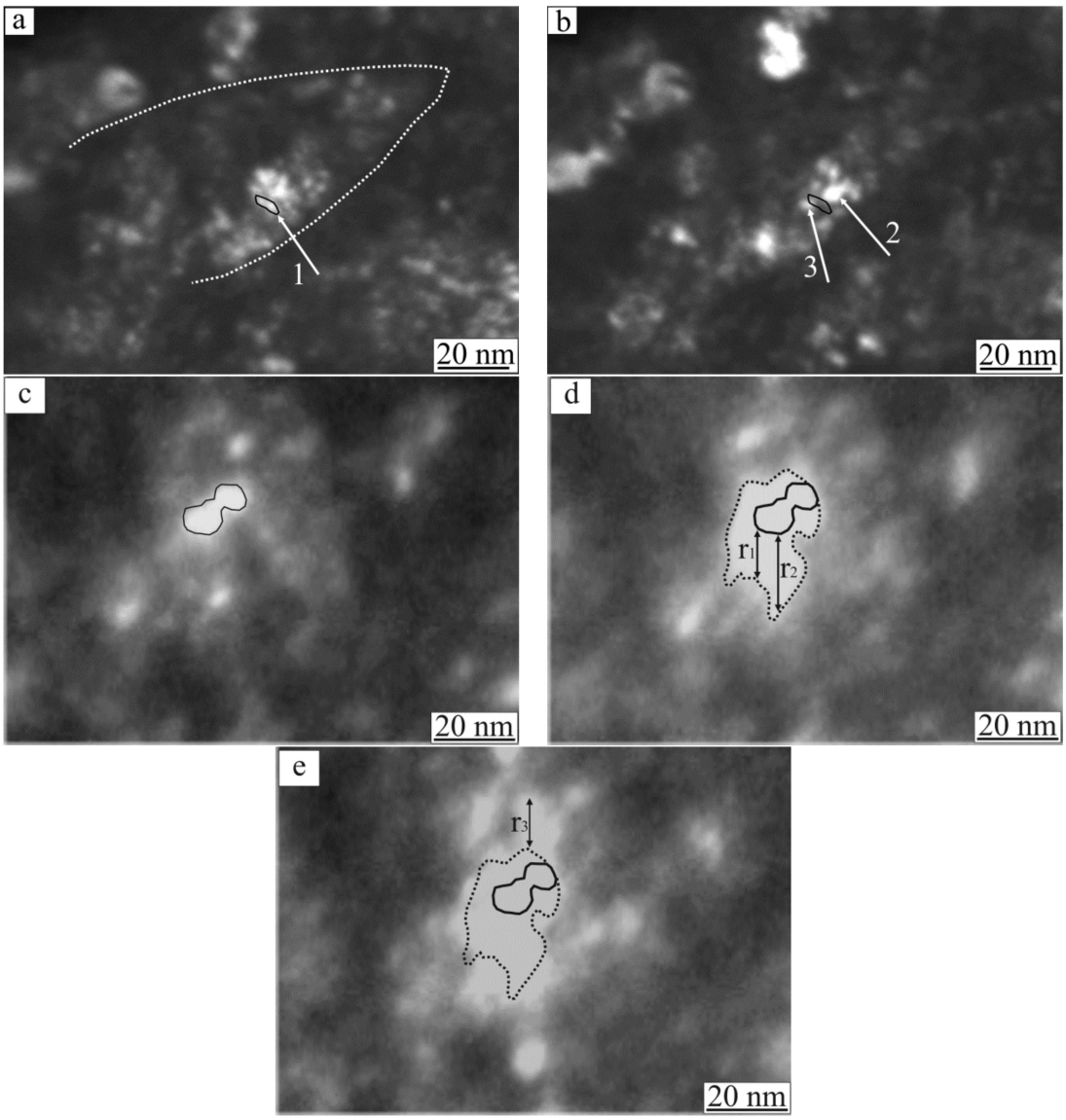

Figure 13. Dark-field images of extinction contour displacement in the bulk of the submicrocrystalline structure under the indenter's tip: (**a**,**b**) dipole misorientation of the crystals: **a**—sample angle tilt 0°, **b**—sample angle tilt 0.3°; (**c**–**e)** the relaxed structure state: **c**—sample angle tilt 0°, **d**—sample angle tilt 0.3°, **e**—sample angle tilt 0.6° (see explanation in text).

As shown by the comparison of the dark-field images of extinction contour positions (denoted by the dark line, arrow 1 and arrows 2 and 3) at different sample inclination angles by 0.3°, the noted crystals had a small-angle misorientation of reflecting planes of the <220> type, while crystals 2 and 3 (Figure 13b) had the same orientation. This means that when passing from crystal 1 to crystal 2 through the crystal enclosed in the dark line, the rotation vector of these planes was inverted. Hence, we had the same situation of dipole misorientation of crystals as considered above (Figure 11).

Due to the small dislocation of extinction contours due to the inclination, such a structure state attained large bending of the crystal lattice (up to 130° μm^{-1}). However, similar

relaxed structure states could be detected (Figure 13c–e). In this case, with inclination to the same angle (≈0.3°), the contour displacements were multiple times higher, though their values could be different in different directions and different regions (as denoted in Figure 13 by arrows r_1 and r_2). This reflected the nonuniformity of the stress–strain state at the scales of such displacements (in the example, nearly 1.5-fold as compared to the crystal lattice bending–torsion). In certain regions, for example, near arrow r_3, there was only a partial displacement of the contour, which testified to the formation of a small-angle discrete misorientation boundary near the non-displaced contour edge.

Thus, the presented results showed that in the indentation zone under the indenter's tip, the deformation of layers with initially different structures led to leveling out the characteristics of their structure state (parameter and bending of the crystal lattice) and causing their defect structures to be similar: formed nanosized misoriented crystals with dipoles and nonuniform misorientations. We should also note the role of crystal boundaries as the sources of deformation (increased bending of the crystal lattice in their region) and the increased number (or their relative fraction of extension) of misorientation boundaries that were perpendicular to the indentation axis and, hence, provided the most effective relaxation of the applied load.

4. Conclusions

This work studied the peculiarities of the after-deposition structure state and deformation via indentation of a gradient-laminated heterophase cermet coating. In the coating growth, we found a peculiarity of the structure state (surface relief smoothing during the transition from a columnar to a nanocrystalline structure) and alteration of the elemental composition (a drop in the concentration of nitride-forming elements and increase in the concentrations of Al and Si at a constant target sputtering power), which could be conditioned by the effect of secondary sputtering of the coating surface, in combination with the negative influence of copper on the stability of the titanium nitride phase.

The coating fracture behavior was studied. It was established that near the indenter's tip, the nanocrystalline structure experienced the formation of separate nanosized localized fracture areas connected by multiple branching cracks, which possibly impeded the development of a macro-fracture in that region. It was shown that coarse micro- and submicroscale cracks occurred in the locations of stress concentrators (indent ridges) and prolonged structure defects (layer interfaces). There were no displacements along the boundaries of columnar crystals and no radial cracks along those boundaries in the region of coating coupling with the substrate.

The macroscopic plastic deformation of the individual coating layers was estimated in this work based on the measurements of the indentation profile. It was established that the deformation of both layers amounted to dozens of percent, and more in magnitude, especially with increasing distance from the top, for a layer with a columnar structure. The deformation value throughout the indent cross-section had different signs for both layers, which testified to mass transfer at the scale of the indent in the direction normal to the loading axis. Taking into account these data and due to preserved flat surface of the substrate in the indent region, it could be hypothesized that the correlation of the properties of this coating and substrate (T15K6 alloy) explained the indentation energy absorption through plasticity and fracture of the coating.

The characteristics of the microstructure of different coating layers in the indentation zone were studied. It was shown that in the submicrocrystalline region, the deformational alterations of the structure under the tip were expressed as the fracture of the columnar structure through the formation of a multitude of interfaces that were transverse to the growth direction. This led to the formation of an equiaxial crystalline structure in this region with crystal dimensions of up to 100 nm. Evidently, in this case, the boundaries were of deformational origin. Moreover, near the tip on the side faces of the indent, there was an inclination of the boundaries of columnar crystals.

The dark-field transmission electron microscopy demonstrated that in the indentation zone under the indenter's tip, the deformation of layers with initially different structures both leveled out the characteristics of their structure state (parameter and bending of the crystal lattice) and caused their defect structure to be similar: formed nanosized misoriented crystals with dipole and nonuniform misorientations.

We should also note the role of crystal boundaries as the sources of deformation (increased bending of the crystal lattice in their region) and the increased number (or their relative fraction of extension) of misorientation boundaries that were perpendicular to the indentation axis and, hence, provided the most effective relaxation of the applied load.

Author Contributions: S.O.: conceptualization, methodology, investigation and writing—original draft preparation; V.K.: conceptualization, investigation, resources and funding acquisition. All authors have read and agreed to the published version of the manuscript.

Funding: The work was performed according to the government research assignment for ISPMS SB RAS, project no. FWRW-2021-0003.

Institutional Review Board Statement: Not applicable.

Informed Consent Statement: Not applicable.

Data Availability Statement: The data presented in this study are available on request from the corresponding author.

Acknowledgments: We are grateful the Tomsk Materials Science Center for Collective Use of the Tomsk State University and the Nanotech Center for Collective Use of the Institute of Strength Physics and Materials Science, Siberian Branch, Russian Academy of Sciences for the opportunity to use their equipment.

Conflicts of Interest: The authors declare no conflict of interest.

References

1. Veprek, S.; Veprek-Heijman, M.G.J.; Karvankova, P.; Prochazka, J. Different approaches to superhard coatings and nanocomposite. *Thin Solid Films* **2005**, *476*, 1–29. [CrossRef]
2. Jayaram, V.; Bhowmick, S.; Xie, Z.H.; Math, S.; Hoffman, M.; Biaswas, S.K. Contact deformation of TiN coatings on metallic substrates. *Mater. Sci. Eng. A* **2006**, *423*, 8–13. [CrossRef]
3. Ma, L.W.; Cairney, J.M.; Hoffman, M.; Munroe, P.R. Deformation mechanisms operating during nanoindentation of TiN coatings on steel substrates. *Surf. Coat. Technol.* **2005**, *192*, 11–18. [CrossRef]
4. Carvalho, N.J.M.; De Hosson, J.T.M. Deformation mechanisms in TiN/(Ti,Al)N multilayers under depth-sensing indentation. *Acta Mater.* **2006**, *54*, 1857–1862. [CrossRef]
5. Molina-Aldarequia, J.M.; Lloyd, S.J.; Oden, M.; Joelsson, T.; Hultman, L.; Clegg, W.J. Deformation structures under undentation in TiN/NbN single-crystal multilayers deposited by magnetron sputtering at differing bombarding ion energies. *Philos. Mag. A.* **2002**, *82*, 1983–1992. [CrossRef]
6. Xie, Z.H.; Hoffman, M.; Moon, R.J.; Munroe, P.R. Deformation of a hard coatings on ductile substrate system during nanoindentation: Role of the coating microstructure. *J. Mater. Res.* **2006**, *21*, 437–447. [CrossRef]
7. Verma, N.; Cadambi, S.; Jayaram, V.; Biswas, S.K. Micromechanisms of damage nucleation during contact deformation of columnar multilayer nitride coatings. *Acta Mater.* **2012**, *60*, 3063–3073. [CrossRef]
8. Xie, Z.H.; Hoffman PMunroe, M.; Bendavid, A.; Martin, P.J. Deformation mechanisms of TiN multilayer coatings alternated by ductile or stiff interlayers. *Acta Mater.* **2008**, *56*, 852–861. [CrossRef]
9. Wu, Z.T.; Qi, Z.B.; Zhang, D.F.; Wang, Z.C. Nanoindentation induced plastic deformation in nanocrystalline ZrN coating. *Mater. Lett.* **2016**, *164*, 120–123. [CrossRef]
10. Roa, J.J.; Jiménez-Piqué, E.; Martinéz, R.; Tarrado, J.M.; Rodríquez, R.; Leanes, L. Contact damage and fracture micromechanisms of multilayered TiN/CrN coatings at micro- and nano-lenght scales. *Thin Solid Films* **2014**, *571*, 308–315. [CrossRef]
11. Wu, Z.; Zhong, X.; Wang, Z.; Dai, W.; Wang, Q. Plastic deformation induced by nanoindentation test applied on ZrN/Si_3N_4 multilayer coatings. *Coatings* **2018**, *8*, 11. [CrossRef]
12. Yalamanchili, K.; Forsén, R.; Jiménez-Piqué, E.; Johansson Jöesaar, M.P.; Roa, J.J.; Ghafoor, N.; Odén, M. Structure, deformation and fracture of arc evaporated Zr-Si-N hard films. *Surf. Coat. Technol.* **2014**, *258*, 1100–1107. [CrossRef]
13. Bigelow, S.; Shen, S.-L. Parametric computational analysis of indentation-induced shear band formation in metal-ceramic multilayer coatings. *Surf. Coat. Technol.* **2018**, *350*, 779–787. [CrossRef]
14. Oliver, W.C.; Pharr, G.M. An improved technique for determining hardness and elastic modulus using load and displacement sensing indentation experiments. *J. Mater. Res.* **1992**, *7*, 1564–1583. [CrossRef]

15. Korotaev, A.D.; Tyumentsev, A.N.; Sukhovarov, V.F. *Disperse Hardening of Refractory Metals*; Science: Novosibirsk, Russia, 1989; p. 210.
16. Tyumentsev, A.N.; Korotaev, A.D.; Pinzhin, Y.P. Highly defective structural states, local internal stress fields and and cooperative mechanisms of the mesoscale deformation and crystal reorientation in nanostructured metallic materials. *Phys. Mesomech.* **2004**, *7*, 35–53.
17. Patsalas, P.; Abadias, G.; Matenoglou, G.M.; Koutsokeras, L.E.; Lekka, C.E. Electronic and crystal structure and bonding in Ti-based ternary solid solution nitrides and Ti-Cu-N nanocomposite films. *Surf. Coat. Technol.* **2010**, *205*, 1324–1330. [CrossRef]
18. Ovchinnikov, S.V.; Pinzhin, Y.P. Growth structure and properties of gradient nanocrystalline coatings of the Ti-Al-Si-Cu-N system. *Russ. Phys. J.* **2016**, *56*, 799–808. [CrossRef]
19. Cavaleiro, A.; De Hosson, J.T.H. *Nanostructured Coatings*; Springer: New York, NY, USA, 2006; p. 651.
20. Vaz, F.; Rebouta, L.; Goudeau Ph Girardeau, T.; Pacaud, J.; Riveire, J.P.; Traverse, A. Structural transitions in hard Si-based TiN coatings: The effect of bias voltage and temperature. *Surf. Coat. Technol.* **2001**, *146–147*, 274–279. [CrossRef]
21. Zha, X.; Jiang, F.; Xu, X. Investigation of modelling and stress distribution of a coating/substrate system after an indentation test. *Int. J. Mech. Sci.* **2017**, *134*, 1–14. [CrossRef]
22. Ovchinnikov, S.V.; Korotaev, A.D.; Pinzhin, Y.P. Modification of the microstructure of TiN based columnar coatings in indentation zones. *Russ. Metall.* **2015**, *2015*, 278–284. [CrossRef]